Energy & Environmental Science

Cite this: DOI: 10.1039/c9ee00956f

Expanded hydrated vanadate for high-performance aqueous zinc-ion batteries†

Chaofeng Liu, Zachary Neale, Jiqi Zheng, Xiaoxiao Jia, Juanjuan Huang, Mengyu Yan, Meng Tian, Mingshan Wang, Jihui Yang* and Guozhong Cao*

Received 24th March 2019,
Accepted 14th May 2019

DOI: 10.1039/c9ee00956f

rsc.li/ees

Hydrated vanadates are promising layered cathodes for aqueous zinc-ion batteries owing to their specific capacity as high as 400 mA h g^{-1}; however, the structural instability causes serious cycling degradation through repeated intercalation/deintercalation reactions. This study reveals the chemically inserted Mn(II) cations act as structural pillars, expand the interplanar spacing, connect the adjacent layers and partially reduce pentavalent vanadium cations to tetravalent. The expanded interplanar spacing to 12.9 Å reduces electrostatic interactions, and transition metal cations collectively promote and catalyze fast and more zinc ion intercalation at higher discharge current densities with much enhanced reversibility and cycling stability. Manganese expanded hydrated vanadate (MnVO) delivers a specific capacity of 415 mA h g^{-1} at a current density of 50 mA g^{-1} and 260 mA h g^{-1} at 4 A g^{-1} with a capacity retention of 92% over 2000 cycles. The energy efficiency increases from 41% for hydrated vanadium pentoxide (VOH) to 70% for MnVO at 4 A g^{-1} and the open circuit voltage remains at 85% of the cutoff voltage in the MnVO battery on the shelf after 50 days. Expanded hydrated vanadate with other transition metal cations for high-performance aqueous zinc-ion batteries is also obtained, suggesting it is a general strategy for exploiting high-performance cathodes for multi-valent ion batteries.

Broader context

Aqueous zinc ion batteries with nonflammable electrolytes offer high safety, fast charge/discharge capability, long-term cycling stability, and low cost with a comparable energy density to lithium ion batteries. However, the lack of cathodes with high practical capacity, high discharge voltage, low self-discharge, and cycling stability remains an imperative challenge. Hydrated vanadium pentoxide (VOH) delivers a specific capacity as high as 400 mA h g^{-1} but suffers from structural degradation because of the weak van der Waals forces between the layers. In the present work, divalent transition metal cations (TMs) were chemically pre-inserted into VOH, resulting in a much larger storage capacity and a higher discharge voltage, and enhanced rate capability and cycling stability in comparison with VOH owing collectively to an enlarged interplanar spacing, a stabilized crystal structure, a catalytic effect, and improved charge and ion transport properties. The increased energy efficiency and reduced voltage degradation reveal great potentiality for commercial applications.

Introduction

Layered materials offering sufficient intercalation channels and active sites for working cation transportation and accommodation have become the most competitive electrode materials for supporting commercial applications of rechargeable batteries,[1–7] especially secondary Li ion batteries based on lithium cobalt oxide and graphite, which have brought a revolution to portable electronics and communication.[8–11] However, layered cathodes in flammable and highly volatile nonaqueous electrolytes introduce serious safety issues when oxygen released from the layered cathode penetrates to the anode causing thermal runaway.[12] Aqueous electrolytes endow rechargeable batteries with improved safety protection, but the limited voltage window and single-electron carriers seriously restrain the energy density of batteries, even if high concentration salt solutions and "water-in-salt" electrolytes were introduced in Li-ion systems.[13,14] Multivalent ions such as Mg^{2+},[15] Zn^{2+},[16] Ca^{2+}[17] and Al^{3+}[18] carry more charges per ion than Li^{+} or Na^{+} and are believed to be promising working ions in rechargeable batteries. Among all multivalent ions mentioned above, Zn^{2+} has a smaller ionic radius of 0.88 Å in six-fold coordination and the Zn metal anode has a high volumetric capacity around 5850 mA h cm^{-3}, thus aqueous zinc ion batteries (AZIBs) have become a hot research field.[16,19–21] Before any new breakthrough happens in the present voltage-limited aqueous electrolytes, exploiting cathodes with high

Department of Materials Science and Engineering, University of Washington, WA, USA. E-mail: jihuiy@uw.edu, gzcao@uw.edu

† Electronic supplementary information (ESI) available. See DOI: 10.1039/c9ee00956f

specific capacity is an effective way to achieve an increase in battery energy density.

Cathode materials for ZAIBs mainly include manganese oxides,[22–28] vanadium oxides,[29–36] Prussian blue and its analogues,[37–40] transition metal dichalcogenides[41–44] and organic compounds.[45,46] Manganese dioxides can be classified into one-, two- and three-dimensional tunnel structures that influence their electrochemical activities for Zn ion storage.[16,19] The partially irreversible phase transition and the dissolution of active materials cause unstable cycling performance.[21,24,47] Prussian blue, a mixed-valence hexacyanoferrate with an open framework, has a tunable lattice spacing through introducing different transition metal cations,[38,48] but the lower specific capacity of <100 mA h g^{-1} makes its uncompetitive in comparison with manganese oxides of 300 mA h g^{-1}.[16,19] Dichalcogenides deliver a considerable specific capacity around 200 mA h g^{-1}, however, the intrinsically low electrical conductivity and discharge voltage restrain their energy density and efficiency.[44,49] Although organic compounds present a promising Zn ion storage capability, the dissolvable species formed in the cycling process cause rapid capacity fading.[45] Layered vanadate compounds as one of the cathode categories for Zn-ion batteries can deliver a specific capacity as high as 400 mA h g^{-1} owing to the variable chemical valence of vanadium ions from 5+ to 3+ and their tunable interlayer distance for Zn-ion access and diffusion.[16,21] Additionally, vanadium element has a considerable abundance of 190 ppm in the Earth's crust, leading to a lower cost than that of cobalt, widely used in commercial Li-ion batteries.[50] Layered vanadium pentoxide, a common cathode for Li- and Na-ion batteries, in aqueous Zn ion batteries delivered an increasing cycling gravimetric capacity due to the exfoliation of the initial chunks to allow more reactive sites.[30] Hydrated vanadium pentoxide ($V_2O_5{\cdot}nH_2O$, VOH) has a bilayer structure and structural water molecules work as the pillar to expand the layer spacing to near 12 Å. More importantly, the shielding effect from water decreases the interaction between cations and plays a role to accelerate Zn ion diffusion.[51] In order to improve the reaction kinetics of VOH, an essential strategy is to introduce some alien cations into the interlayers to enlarge the spacing. It was found that a bigger radius of the alien cations could produce a larger layer distance and obtain faster ion diffusion. For example, hydrated Mg^{2+} with a radius of 4.3 Å creates an interlayer spacing of 13.4 Å in VOH, which is larger than the 11.07 Å in hydrated Li^+ expanded VOH because hydrated Li^+ has a smaller radius of 3.8 Å.[52,53] Similar studies have also been done with preinserted calcium and zinc cations.[36,54] However, the introduced cations just play a role in expanding the lattice spacing to accelerate the ion diffusion; the electrochemical stability of the host materials still suffers from structural degradation, especially with the possibility that alien cations deintercalate during the cycling processes because of the weak van der Waals interactions between hydrated alien cations and oxygens from the layered slabs of the host. Compared with the weak interactions, the ideal situation is chemical bonding to lock the layered slabs and endow the host material with stable cycling stability for intercalation/deintercalation reactions without sacrificing the interplanar spacing.

In this paper, Mn(II) cation expanded hydrated vanadium pentoxide (MnVO) is prepared through a hydrothermal method and shows a much larger storage capacity and higher discharge voltage, and enhanced rate capability and cycling stability in comparison with VOH owing collectively to an enlarged interplanar spacing, a stabilizing effect from Mn(II) pillars, a catalytic effect, and improved charge and ion transport properties. The increased energy efficiency and reduced voltage degradation reveal great potentiality for commercial applications. More importantly, other transition metal cations (TMCs), such as Co and Ni, are also introduced and present the same structures and functionality to enhance the Zn-ion storage performance in an aqueous system, implying introducing TMCs is an effective and general strategy for improving the layered VOH cathode.

Experimental

All chemicals were used as received without purification. 2 mmol of V_2O_5 (99.6+%, Sigma-Aldrich) was dissolved into 50 mL of DI H_2O with 2 mL of H_2O_2 (30%, Fisher Chemical), and 1 mmol of $MnSO_4{\cdot}10H_2O$ (98.3%, Fisher Scientific) was dissolved separately into 30 mL of DI water. The two solutions were admixed and transferred to a 100 mL (internal diameter of 42 mm with a height of 72 mm) Teflon lined stainless steel autoclave and heated to and held at 120 °C for 6 h. Brick red precipitates were collected by centrifugation and washed with water and ethanol three times. The collected precipitates were dried at 70 °C overnight in an electric oven and turned greenish. The resulting product (MnVO) was further dried at 120 °C in a vacuum oven. VOH was synthesized with the same procedure and processing conditions without Mn(II) sources, 80 mL of DI water was used in order to attain the same internal reaction pressure in the Teflon bottle and the resulting product was dried using a freeze dryer at −52 °C. For Co(II) and Ni(II) stabilized samples, their sulfate salts were used to synthesize the desired samples and the processes were identical to the MnVO synthesis.

Phase identification was carried out using a Bruker X-ray diffractometer (D8 Discover with a IμS 2-D detection system) at an accelerating voltage of 50 kV and a working current of 1000 μA. A Fourier transform infrared spectrometer (FT-IR, Bruker, VERTEX 70) was used to collect the functional groups' stretching or bending information from 400 to 4500 cm^{-1} and a Renishaw InVia Raman microscope equipped with a Leica DMIRBE inverted optical microscope was also used to obtain chemical bond information using one of the laser excitation sources at 514 nm. A differential scanning calorimeter (DSC 3+ STAR^e System, Mettler Toledo) was adopted to analyze the thermal stability of the sample within 40–700 °C in flowing nitrogen gas (50 sccm). The microstructures of the samples were observed using a scanning electron microscope (SEM, FEI Sirion) at a working voltage of 5 kV and a scanning transmission electron microscope (S/TEM, Tecnai G2 F20) with an accelerating voltage of 200 kV. The surface chemical states of the samples were determined using a Kratos Axis Ultra DLD X-ray Photoelectron Spectroscopy system (XPS) with an AlKα radiation

source that was operated at 10 mA and 15 kV, and with a charge neutralizer. The angle between the specimen normal and the spectrometer was 0°.

For the electrode preparation, the active material was mixed with conductive carbon and polyvinylidene fluoride (PVDF) binder in a weight ratio of 7 : 2 : 1 in *N*-methyl-2-pyrrolidone (NMP) solvent to obtain a slurry that was pasted on a current collector – titanium foil. The prepared electrodes were dried in a vacuum oven at 120 °C overnight. The mass loading of active materials is 3–4 mg cm^{-2}. Zn metal was used as the anode and 80 μL of 3 M zinc trifluoromethanesulfonate (98%, $Zn(CF_3SO_3)_2$) aqueous solution was injected into the batteries as the electrolyte. A glass fiber filter (Whatman, Grade GF/A) was used as the separator. The redox characteristics of the cathodes were tested by cyclic voltammetry (CV) on a Solartron electrochemical station (SI 1287) equipped with an electrochemical impedance spectroscopy system (EIS, SI 1260). The galvanostatic intermittent titration technique (GITT) was applied to analyze the reaction and diffusion kinetics at a current density of 50 mA g^{-1} and a charge/discharge time and interval of 10 min for each step. The galvanostatic charge and discharge tests were conducted using a Neware tester (CT-4008). The working voltage of the cells was set from 0.2 to 1.6 V *versus* Zn^{2+}/Zn, and the EIS measurements have a frequency range between 10^5 and 0.01 Hz.

Results and discussion

Fig. 1a compares the XRD patterns of MnVO and VOH, in which VOH is well indexed with the standard peaks ($V_2O_5{\cdot}nH_2O$, PDF 40-1296) and MnVO shows the same diffraction peaks as reported $M_xV_2O_5A_y{\cdot}nH_2O$ (M = cations, A = anions).[55] However, the Miller indices corresponding to the crystallographic planes do not exist in the current database. The structure of $M_xV_2O_5A_y{\cdot}nH_2O$ is believed to consist of stacked V–O double layers and the adjacent layers are separated by water and cations and anions added in the preparation.[55] The strongest peak at 6.8° in MnVO corresponds to a larger lattice spacing of 12.9 Å and VOH has the strongest peak at 7.4° with a lattice spacing of 11.9 Å, which agrees with the reported ~11.5 Å,[56] suggesting the introduction of Mn(II) with water together can expand the interlayer spacing further as reported in preinserted Mg VOH.[52] In the FTIR spectra (Fig. 1b), the peaks at 461 and 737 cm^{-1} originate from the symmetric stretching vibration of the O–V–O bonds and the peak located at 992 cm^{-1} is attributed to the stretching vibration of the V=O bonds.[57] The bending and stretching vibrations of O–H from structural water appear around 1612 and 3450 cm^{-1},[58] respectively. Upon careful examination, a slight red-shift (2–5 cm^{-1}) of V–O vibrations appears in MnVO in comparison with VOH, suggesting the V–O bond becomes weak because a fraction of V^{5+} is reduced to V^{4+} in MnVO;[59] the details on chemical states will be discussed further with the XPS results. The similarity in the FT-IR spectra reveals similar crystal structures in both samples. Raman spectra (Fig. 1c), as complementary fingerprints of the samples to the FT-IR spectra, were collected. The peak located at 159 cm^{-1} comes from the bending vibration of the –O–V–O–V– chains, which implies an *a*-directional compressive deformation in the lattice.[60] A blue shift of 4 cm^{-1} in MnVO verifies the stronger compression along the *a*-direction due to the possible electrostatic interaction between Mn(II) and O. The bending vibration of the V=O bond formed by terminal O and the center V cation appears at 264 cm^{-1},[61] and the red shift of 4 cm^{-1} in MnVO means the elongation of V=O along the *c*-direction, consistent with the XRD results of the lowest angle. The broad peak around 352 cm^{-1} is related to the librational motions of water.[62] The triply coordinated O_3 by three V cations forms a V_3–O bond that connects three edge sharing VO_5 pyramids in the crystal structure[56] and is reflected by a stretching signal at 512 cm^{-1} [61] and a red shift of 5 cm^{-1} in MnVO suggests a lattice expansion along the *b*-direction. The bridging O links two corner-sharing VO_5 polyhedra and the stretching vibration of V_2–O appears at 706 cm^{-1},[61,63] and the peak at 674 cm^{-1} from stretching of V_2–O suggests a partially disordered V–O–V connection existing in the host lattice.[63] The weakened peak at 674 cm^{-1} in MnVO reveals better crystallinity and the possible reason is that the introduced Mn(II) makes the arrangement of V and O more orderly because of the interaction among the three ionic species. The peak at 891 cm^{-1} is attributed to the stretching of V–OH_2.[64] A weakened V–OH_2 bond appears in MnVO because of the red shift, which implies water has more rotational freedom in the interlayer.[62] The competing interaction from Mn(II) and water could influence the bond strength of V–OH_2. Compared the spectra of 600–800 cm^{-1} of both samples, a broad peak appears at 674 cm^{-1} in MnVO rather than the sharp peak in VOH. Lorentz functions were used to obtain the details of chemical bonds; two discernable peaks at 674 and 706 cm^{-1} fit well with the stretching of V_2–O in VOH (Fig. 1d), and a weak peak at 652 cm^{-1} corresponds to the vibration of Mn–O bonds in the MnO_6 octahedra of MnVO (Fig. 1e),[65] suggesting that Mn(II) ions connect $[VO_n]$ layers by chemical bonds. It should be mentioned that the bending or stretching signal of sulfate anions is not detected in Raman or FT-IR spectra, demonstrating no sulfate anions in MnVO. Based on the structural comparison, it can be speculated that MnVO has two possible structures. One is the bi-layer structure in which Mn(II) cations reside in the interlayers like a slight structure distortion in VOH; it can be caused by a pre-inserted cation such as sodium in V_2O_5.[66] The other is to form a new phase such as $MnV_{12}O_{31}{\cdot}10H_2O$ (PDF 47-0146)[67] which has the same XRD pattern as $M_xV_2O_5A_y{\cdot}nH_2O$ but no crystal structure details can be found in the current database. For the former, preinserted cations, such as Li^+ [53] and Mg^{2+},[52] in VOH seldom cause a big difference in the XRD patterns. The changes in the XRD pattern mean the formation of new phases, but the analysis based on the FT-IR and Raman spectra demonstrate both samples have similar chemical bonds. Combining the structural information discussed above, MnVO is likely to have a similar crystal structure to VOH and the preinserted Mn(II) in the interlayer forms the chemical bonds.

Fig. 2a shows TEM images in which MnVO consists of nanosheets. The nanosheets aggregate to form a micro-flower-like shape as observed by SEM (Fig. S1, ESI†). EDS mapping collected by TEM exhibits homogeneous element distributions of Mn, V and O in the resulting MnVO sample, and the lattice

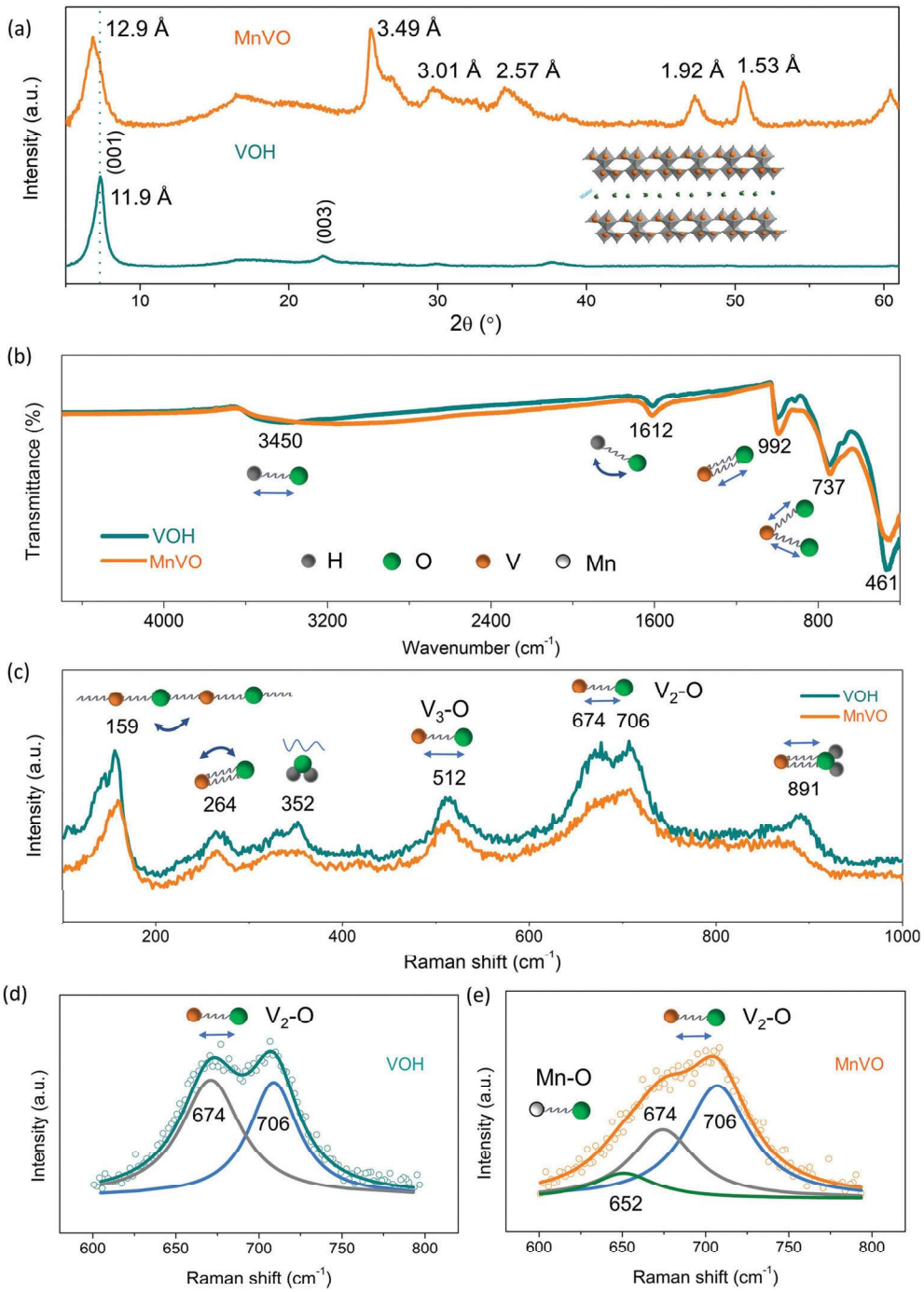

Fig. 1 (a) XRD patterns of MnVO and VOH. (b) FT-IR and (c) Raman spectra of MnVO and VOH, the vibrations from V–O, O–H, and water are detected. The similarity of both spectra demonstrated MnVO has a similar structure to VOH. However, the changed chemical bonds indicate the introduced Mn(II) likely sits in the interlayers. The partially fitted Raman spectra of (d) VOH and (e) MnVO. The peak at 652 cm^{-1} corresponding to Mn–O in MnO_6 octahedra demonstrates a chemical connection formed between Mn(II) and O.

spacing of 12.9 Å is in accordance with the XRD results. No sulfur was detected, which supports the argument about no anions (SO_4^{2-}) in MnVO interlayers as mentioned in the structural analysis. To confirm the effects of Mn(II) on the structural stability, DSC/TGA is used to analyze the water loss and possible phase transition in the heating process. Water loss in both samples (Fig. 2b) accompanied by a continuous endothermal process is reflected by two weak peaks at 150 and 380 °C and the endothermal peak appearing around 685 °C is attributed to the melting of V_2O_5.[68] It is worth noting that the end temperature for water loss from MnVO (475 °C) is higher than that from VOH (380 °C) as marked by the dotted lines, suggesting water has better structural stability derived from the interaction of Mn in MnVO. The water content in MnVO (15 wt%) is less than that in VOH (17 wt%).

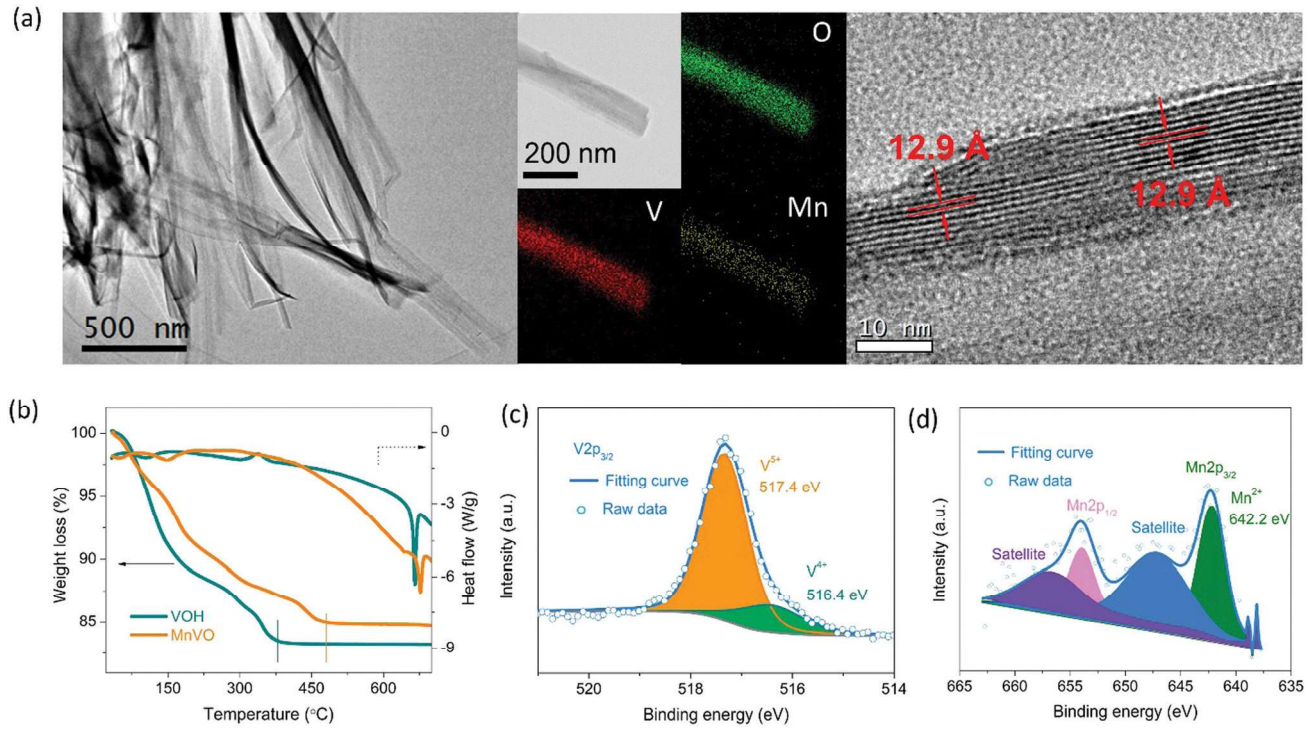

Fig. 2 (a) TEM with EDS mapping and high resolution TEM image of MnVO. The thin nanosheets have homogeneous element distributions and the discernable lattice spacing of 12.9 Å agrees with the XRD data. (b) Differential scanning calorimetry curves from MnVO and VOH, the downward endothermal curve of MnVO suggests MnVO has more stable crystal water. (c) The XPS spectrum of V $2p_{3/2}$ of MnVO and tetravalent vanadium cations was detected and the amount is around 18.9% by calculating the area ratio of the fitted spectra. (d) XPS spectrum of MnVO collected from divalent Mn that demonstrates no redox reaction happened for Mn(II) ions in the synthesis processes.

The introduction of Mn(II) could induce a change in the chemical valence of V^{5+} because of the electroneutrality required in the lattice. Survey XPS spectra (Fig. S2, ESI†) compare the characteristic peaks and the Mn 2p signal is only detected in MnVO, which agrees with the elements in the XRD detected phase. No signal relating to S is detected in either sample, demonstrating no sulfate anions in MnVO and that the structure speculation is reasonable. Characteristic peaks at 517.4 and 517.0 eV in the XPS spectrum of V $2p_{3/2}$ (Fig. 2c) originate from V^{5+}; the difference of binding energy means the local chemical surroundings are different for some V^{5+}, in particular Mn(II) at 642.2 eV (Fig. 2d) and V^{4+} at 516.4 eV were also detected in the literature.[69] The detected divalent state of Mn cations verifies no oxidizing reaction happens for Mn(II) in the synthesis processes. The ratio of V^{4+} in MnVO and VOH is 18.9% and 13.2% (Fig. S3, ESI† and Fig. 2c), respectively, determined by evaluating the integrated area in the fitted spectra. The appearance of V^{4+} in VOH is possibly from a reduction reaction between V_2O_5 and H_2O_2 to form $VO(O_2)^+$ in the synthesis process.[70] More V^{4+} detected in MnVO is attributed to the introduced Mn(II) and the appearance of V^{4+} implies oxygen vacancies in VOH and MnVO as reported in V_2O_5 or VOH.[71,72] The impacts from oxygen vacancies are close in both samples because of the similar amounts of V^{4+}, thus the differences in electrochemical performance are derived from the introduced Mn(II). V^{4+} has a bigger ionic radius of 72 pm compared to that of 68 pm for V^{5+} in six coordination, which further expands the lattice spacing. At the same time, Mn(II) and V^{4+} have electrons in their 3d orbitals beneficial for enhancing the electrical conductivity and catalyzing the electrochemical reaction; when Mn(II) cations and oxygen vacancies are introduced, the number of d orbitals located at the bottom of the conduction band and the top of the valence band increases.[72,73] Both samples have a similar surface area of 50 $m^2\ g^{-1}$ (Fig. S4, ESI†), and it is unlikely that their surface area would have significantly different influences on the electrochemical performance.

The redox reaction in MnVO was analyzed by a CV test and two pairs of peaks are shown in Fig. 3a; the peak pair residing at higher voltage (1 V) is related to the redox pair of V^{5+}/V^{4+} and the transition of the V^{4+}/V^{3+} pair appears around 0.5 V.[51,74,75] The overlapped CV curves in the first three cycles mean a reversible reaction of the MnVO cathode in the aqueous Zn-ion battery. An interesting phenomenon is that the first discharge peak around 1 V shifts to a higher voltage in the subsequent cycles, possibly attributed to the local chemical surroundings change after Zn ion insertion. However, VOH has deviating peaks in the first three cycles and the discharge peaks shifts to lower voltage upon cycling (Fig. S5, ESI†). Fig. 3b compares the CV curves of both cathodes collected at 0.1 mV s^{-1} and smaller voltage differences in redox pairs of MnVO are seen as listed in Table 1, meaning the MnVO cathode has a smaller polarization and better reaction kinetics in the electrochemical processes. To analyze the reaction kinetics, various sweeping rates of CV curves were used as shown in Fig. 3c and the cathodic peaks shift toward higher voltages

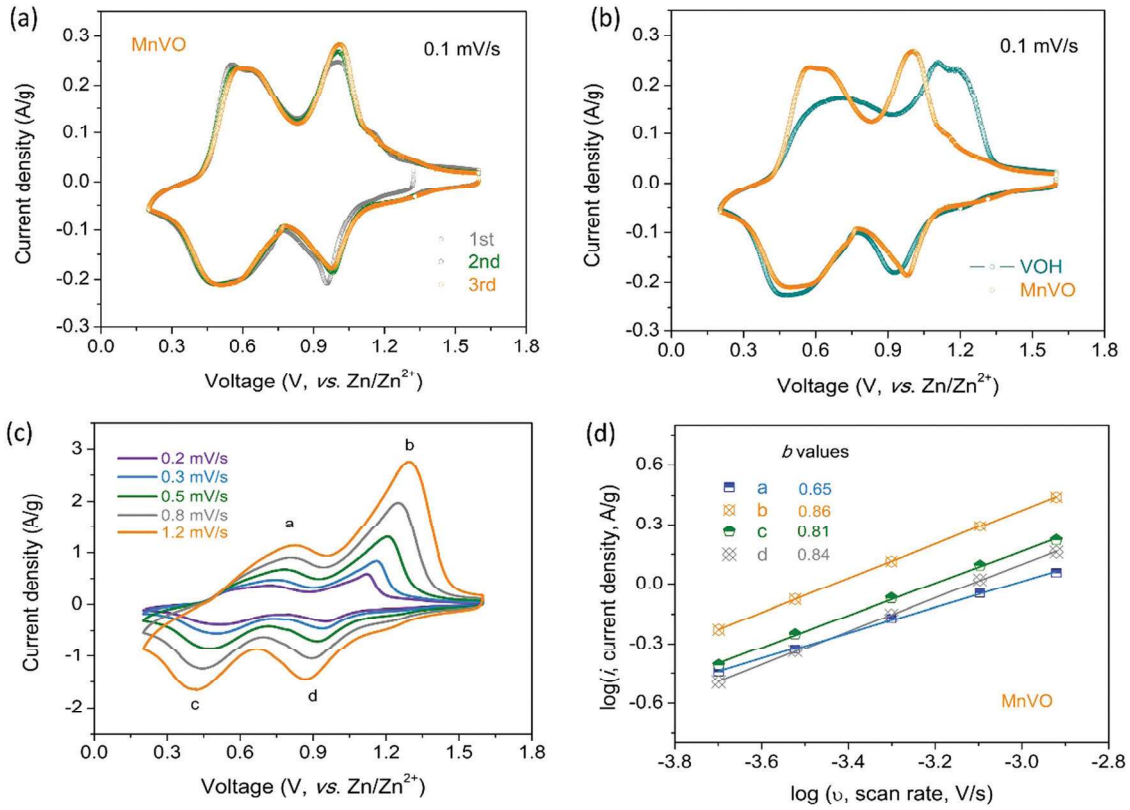

Fig. 3 (a) CV curves of MnVO collected at a sweep rate of 0.1 mV s^{-1}. The overlapping of the curves in the first three cycles means good reaction reversibility in MnVO. (b) Comparison of the CV curves of MnVO and VOH. The smaller voltage deviation in the redox pairs of MnVO suggests better reaction kinetics and reversibility. (c) CV curves of MnVO at various sweep rates and (d) the relationship between peak currents and sweep rates.

Table 1 The redox pairs and voltage differences in both cathode materials

Sample ID	Redox pairs (V)	Differences (V)
VOH	1.15/0.93	0.23
	0.69/0.48	0.11
MnVO	1.01/0.98	0.03
	0.61/0.52	0.09

and the anodic peaks move back to lower voltages with increasing sweeping rate owing to the polarization,[46] especially the phase transition happening in the electrode.[32] Peak currents (i) and sweep rates (ν) obey a power-law relationship that is described by

$$i = a\nu^b, \quad (1)$$

where a and b are variables. A b value of 1 indicates that the surface capacitance dominated the charge storage and 0.5 is indicative of mass diffusion-controlled charge storage.[76–78] The b values of peaks a–d in MnVO are 0.65, 0.86, 0.81 and 0.84 (Fig. 3d), whereas the values of peaks a′–d′ from VOH are 0.65, 0.76, 0.81 and 0.73 (Fig. S6, ESI†). These suggest both samples have considerable kinetics and the electrochemical reactions are limited by ion diffusion and capacitor-like behavior partially contributes to the charge storage.

The voltage profile of MnVO is shown in Fig. 4a and the delivered specific capacity is 415 mA h g^{-1} at a current density of 50 mA g^{-1}, which is higher than that of other vanadium-based cathodes, such as Li intercalated $V_2O_5{\cdot}nH_2O$,[53] $Na_2V_6O_{16}{\cdot}3H_2O$,[34] $H_2V_3O_8$,[79] VO_2,[32,75] LiV_3O_8,[80] or $Mg_xV_2O_5{\cdot}nH_2O$.[52] The sloping curves agree with the board redox peaks in the CV test, and the increased voltage and overlapped curves in the subsequent cycles suggest high reaction reversibility. In the rate capability tests (Fig. 4b), the MnVO electrode with a mass loading of 3–4 mg cm^{-2} delivers an initial specific capacity of 380 mA h g^{-1} at a current density of 0.5 A g^{-1}, and VOH has a capacity of 287 mA h g^{-1}. The difference is that VOH presents a capacity increase to 326 mA h g^{-1} after the first five cycles, but MnVO displays a relatively stable capacity at 371 mA h g^{-1}. With the current density increasing from 1 to 2, 4 and 8 A g^{-1}, MnVO delivers specific capacities of 347, 310, 268 and 214 mA h g^{-1}, respectively, and VOH exhibits capacities of 280, 237, 179 and 124 mA h g^{-1} at the corresponding conditions. The capacity retention in MnVO is 56%, which is higher than that of 38% in VOH, at 8 A g^{-1}, compared with their capacities at 0.5 A g^{-1}; it is also superior in comparison with VO_2[74] and $Mg_xV_2O_5{\cdot}nH_2O$[52] (Table S1, ESI†). When the current densities decrease back to 0.5 A g^{-1} from 8 A g^{-1}, the capacities recover to the initial values, suggesting a stable crystal structure and great electrochemical reversibility. During the high current cycling tests (Fig. 4c), MnVO presents excellent stability after a slight capacity increase owing to the electrolyte penetration and electrochemical activation in the first several cycles.[52] The stable specific capacity is around 260 mA h g^{-1}, which is close to the result from the rate test at the same current density of 4 A g^{-1}.

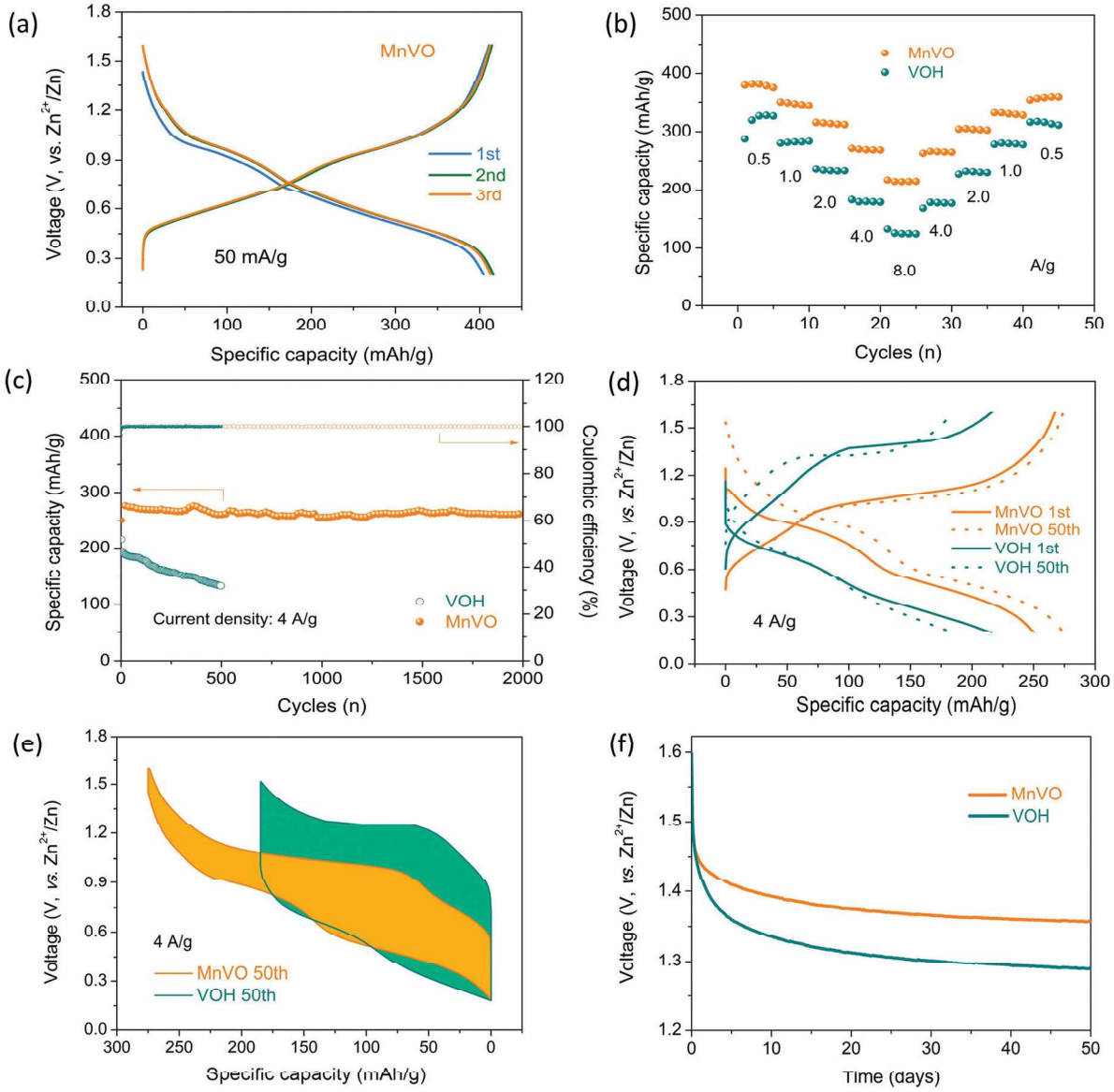

Fig. 4 (a) Voltage profiles of MnVO at 50 mA g^{-1}. (b) Rate capability and (c) cycling stability of both cathodes in the aqueous Zn-ion battery. (d) Voltage profiles at the 1st and 50th cycles collected at 4 A g^{-1}, the smaller polarization and higher energy efficiency in MnVO suggest the introduced Mn(II) cation benefits ion diffusion and stabilizes the crystal structures under fast ion insertion and extraction. (e) Voltage hysteresis of MnVO and VOH collected at 4 A g^{-1} in the 50th cycle. The area encompassed by the charge and discharge curves is the energy loss in the cycle, MnVO displays a smaller energy loss and higher energy efficiency. (f) Open circuit voltage degradation of batteries on the shelf. Less voltage loss means weak self-discharge and stable electrochemical performance.

However, the specific capacity of VOH decreases rapidly and the capacity retention is 66% over 500 cycles, which is lower than the 96% capacity retention over 2000 cycles in MnVO. The capacity retention of MnVO is also higher than that of $Zn_{0.25}V_2O_5{\cdot}nH_2O$ (80% over 1000 cycles at 2.4 A g^{-1})[36] and the $LiV_2(PO_4)_3$ cathode (~75% over 4000 cycles at 1.5 A g^{-1}).[81] The maximum energy and power density of MnVO are 267 W h kg^{-1} and 5791 W kg^{-1}, respectively, which are higher than the 224 W h kg^{-1} and 4244 W kg^{-1} of VOH as shown in the Ragone plot (Fig. S7, ESI†). The voltage hysteresis collected at 4 A g^{-1} exhibits remarkable differences between the two, but this essential indicator for evaluating the practical possibility is ignored in the current reports on zinc ion batteries. As shown in Fig. 4d, MnVO, at the initial cycle(s), delivers a higher specific capacity of 251 mA g^{-1} with a mid-value voltage of 0.61 V, which are higher than the specific capacity of 216 mA h g^{-1} and 0.47 V in VOH. At the 50th cycle, the specific capacity of MnVO has a slight increase to 275 mA h g^{-1} and an increased mid-value voltage of 0.67 V. However, VOH presents a decrease in the specific capacity to 92 mA h g^{-1} with a slightly increased mid-value voltage of 0.51 V. More importantly, the energy efficiency (EE), defined by the ratio of discharge and charge energy densities in the battery performance to evaluate the practicability,[82] is 70% calculated in the 50th cycle of MnVO and its initial EE is 59%.

The hysteresis area encompassed by the charge and discharge curves in Fig. 4e reflects the energy loss in one cycle. A larger area means a lower EE and higher energy loss in the battery. For VOH, it has an initial EE of 40% (Fig. S8, ESI†) and maintains 41% in the 50th cycle, meaning the energy loss reaches up to ~60%. Voltage degradation (Fig. 4f) on the shelf, another practical parameter to evaluate batteries' self-discharge,[83] was also monitored after the full charging process at a current density of 50 mA g^{-1}. The open circuit voltage of the MnVO battery remains at 1.36 V (85% of the cutoff voltage) after 50 days, but VOH degrades to 1.29 V, suggesting less self-discharge reaction happens in MnVO. Generally, the voltage degradation on the shelf comes from the charge redistribution and reverse ion transport between the two electrodes.[84] The better electrochemical performance in MnVO can be attributed to the introduced Mn(II) that combined with water to expand the interlayer spacing for benefiting the ion diffusion to enhance the rate capability and decrease the polarization at a high current density. The Mn(II) cation carries positive charge, which would form a chemical interaction with terminal oxygen from the $[VO_n]$ layers to stabilize the crystal structure, which guarantees structural stability under fast Zn ion insertion and extraction and decreases the ion self-diffusion to restrain the degradation at open circuit voltage when batteries are on the shelf for a long time. In addition, more V^{4+} induced by Mn(II) has a positive effect for improved electrochemical performance owing to its larger ionic radius and one electron in the 3d orbital, which lead to an expanded lattice spacing and enhanced electrical conductivity to catalyze the phase transition.

To confirm the charge storage mechanism, the phase transitions in the electrochemical processes were detected by *ex situ* XRD and the patterns are shown in Fig. 5a. The pristine electrode was fully discharged to 0.2 V; the strongest peak at 6.8° moves to a lower angle of 6.2° meaning the interlayer spacing expanded to 14.1 Å from 12.9 Å. The Zn ion has an ionic diameter of 0.88 Å in six-coordination, but the size of hydrated Zn^{2+} with six water molecules is around 2.1 Å,[85] suggesting Zn ions are desolvated before intercalating. In the fully charged state, the peak at the lowest angle goes back to around the starting position, meaning a highly reversible reaction. The peaks around 35° and 62° present similar tracks. Several weak peaks appear and vanish reversibly in the charging or discharging process, suggesting reversible phases form in the reaction processes. Most V cations reduce from 5+ to 4+ and 3+ when the MnVO cathode is discharged to 0.2 V from pristine as presented in $H_2V_3O_8$.[79] Fig. 5b shows the peak at 517.0 eV corresponding to V^{4+} and 515.9 eV to 3+. The characteristic peak of V^{5+} can be found owing to the incomplete reaction because the delivered specific capacity of 416 mA h g^{-1} at 50 mA g^{-1} (Fig. 4a) is lower than the theoretical capacity of 598 mA h g^{-1} based on the chemical valence of V^{5+} fully reducing to V^{3+} in the reaction. In the fully charged state, V cations are oxidized to 5+ with a small amount of 4+ as found in the pristine state. It is worth noting that the peak position of V^{5+} shifts from 517.4 to 517.6 eV after the full charge (Fig. 5c). In general, the electron binding energy is defined as the extent of the attraction between cations and electrons through electromagnetic forces in a respective atom, ion, molecule or solid, and is determined by the electrostatic force of nuclei and screening effect from neighboring electrons; the formation of chemical bonds causes electron redistribution in atoms or ions and further leads to a change in binding energy.[86] The binding energy shift of V^{5+} to a higher energy state, on one hand, can be attributed to the decrease in the amount of V^{4+} from 18.9% to 10.4% calculated by the area ratio in the simulated XPS results. The amount of V^{4+} decreases and results in a weaker attraction from the nuclei of V^{4+} to the electrons in V^{5+} as observed in hydrogenated V_2O_5.[87] The amount of V^{4+} decrease also explains the capacity increase in the first two cycles as observed in Fig. 4a. The trapped Zn^{2+} (Fig. 5d) is another possible reason because it impairs the electron-withdrawing effect of oxygen from the V cation; the reduced ionic diameter of V^{5+} in comparison with that of V^{4+} means the nucleus has an enhanced interaction with the electrons. The charging specific capacity is higher than the discharging one, which indicates the lower valence V cations are oxidized to 5+ in the first cycle (Fig. 4a) as observed in Fig. 5c. A part of the detected Zn^{2+} in the fully charged state may also come from surface adsorbed or lattice trapped Zn^{2+}.[79,88] Mn(II) was detected by XPS in both the fully discharged and charged states (Fig. S9, ESI†), meaning Mn(II) stays intact in the host crystal. Besides, the oxidation of Mn(II) would occur only at voltages above 1.62 V,[89] thus Mn(II) would not participate in redox reactions at the working voltages of MnVO. EDS mapping in Fig. 5e and f shows the element signals in the fully discharged and charged states; Zn presents a strong and weak signal after discharging and charging in the MnVO cathode, and a reversible stripping/plating reaction simultaneously proceeds on the Zn metal anode as observed by SEM (Fig. S10, ESI†), which means Zn-ion intercalation/de-intercalation reversibly happened in the electrochemical processes. The detected Mn in both states implies it stays stable as a pillar in the crystal lattice. The recovered phases and chemical valence of the constituent elements in the electrochemical processes demonstrate a reversible intercalation reaction for MnVO with the redox pairs from the V cations.

To discern the reasons for the disparity in the electrochemical performance of both samples, GITT plots were collected at a current density of 50 mA g^{-1} as shown in Fig. 6a. The relaxation rest after charging and discharging causes the zigzag voltage profiles and the voltage recovery is used to evaluate the ion diffusion and the IR drop can be transformed to internal reaction resistance (RR).[90,91] The RRs are calculated using the IR drop with the applied current density and the resistances at different steps are shown in Fig. 6b. For MnVO, the RRs are lower than 0.3 Ω g in the whole process, even though a resistance bump appears around 1.0 V in the charging process. However, the RRs of VOH present an increase in the charging process and reach a maximum of 0.9 Ω g around 1.0 V and then go down. In the discharging process, the RRs of MnVO remain stable, but two concave shapes appear at 0.5 and 1.0 V in VOH. It is interesting that the positions of the bumps or concave shapes are identical to the redox peaks observed in CVs (Fig. 3b), implying a radical difference in charge transfer in both samples. From the point of view of crystal structures, charge transfer in VOH prefers to occur along the *ab* plane owing to the

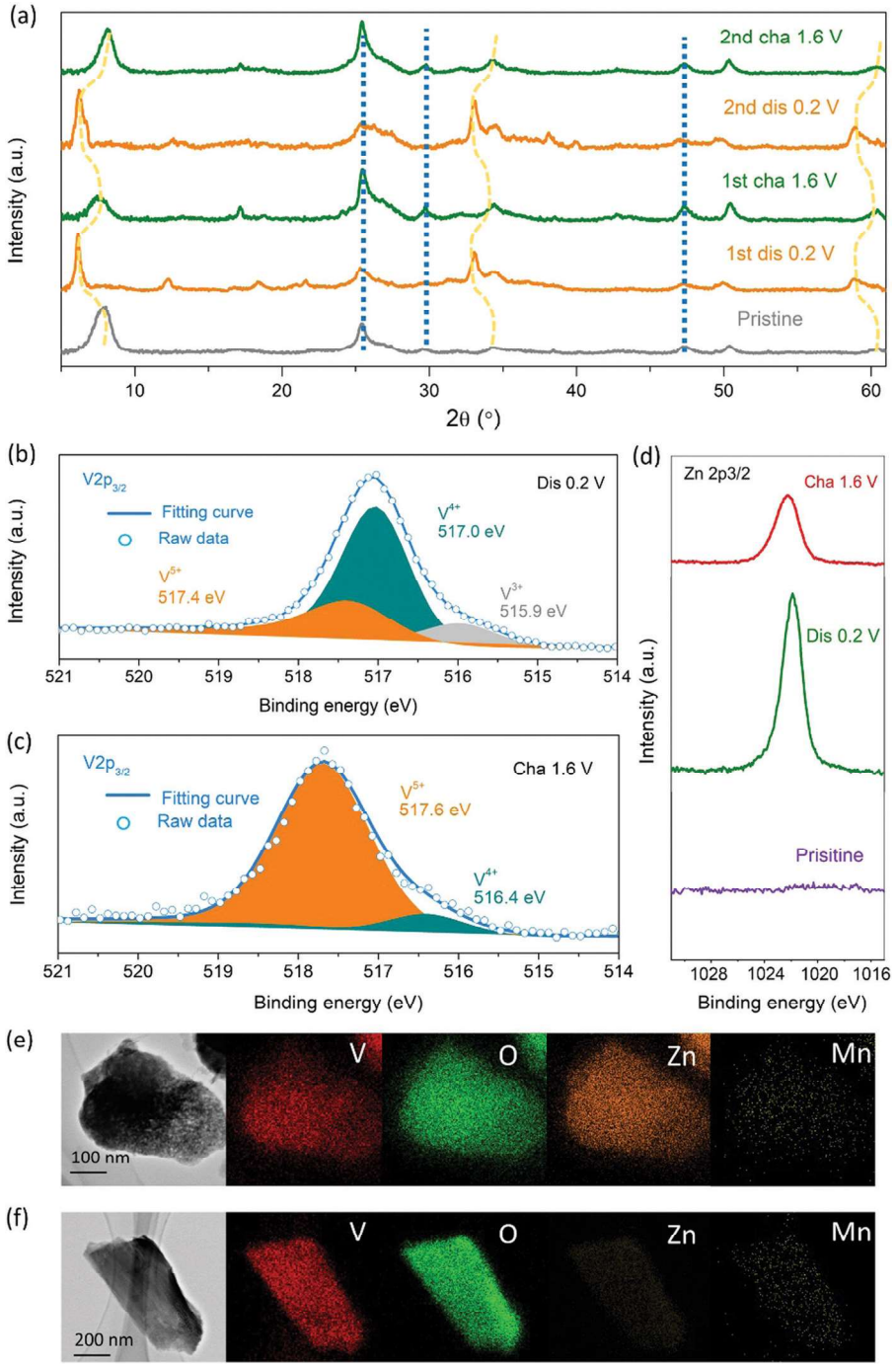

Fig. 5 (a) *Ex situ* XRD patterns of MnVO in the fully discharged and charged states in the initial cycles. The shifts and recovery of the characteristic peaks suggest a reversible intercalation reaction occurring in the electrochemical processes. XPS spectra of V $2p_{3/2}$ in the fully discharged (b) and charged (c) states. The appearance of V^{4+} and V^{3+} agrees with the reduction reaction in the discharge process. V^{5+} dominated compositions in the fully charged state mean the recovery of MnVO and a slight shift of V^{5+} originates from the change of the local chemical surroundings. (d) The evolution of Zn $2p_{3/2}$ spectra in the first cycle. The remaining Zn^{2+} in the fully charged state is attributed to a little trapped Zn^{2+} in the host lattice and surface adsorption even if the disassembled electrode was washed with water several times. TEM images and the corresponding EDS mapping in (e) the fully discharged state and (f) the fully charged state. Mn was detected in both states, suggesting Mn is stable in the crystal lattice. A small amount of Zn ions detected in the fully charged state agrees with results from the XPS spectrum.

$[VO_n]$ polyhedra connected to each other through edge- or point-sharing, but no points or edge contact between the interlayers along the *c*-axis.[56] In MnVO, Mn(II) ions reside between and connect [VO] interlayers so that the charge transfer is 3-dimensional and the charges from the redox reaction can be transferred easily. EIS spectra (Fig. 6c) compare the impedances of batteries before cycling and in the fully charged states and Table 2 lists their charge transfer resistances (CTRs). EIS spectra consist of a semi-circle at the high-frequency region corresponding to charge transfer resistance and a linear tail at low-frequency relating to ion

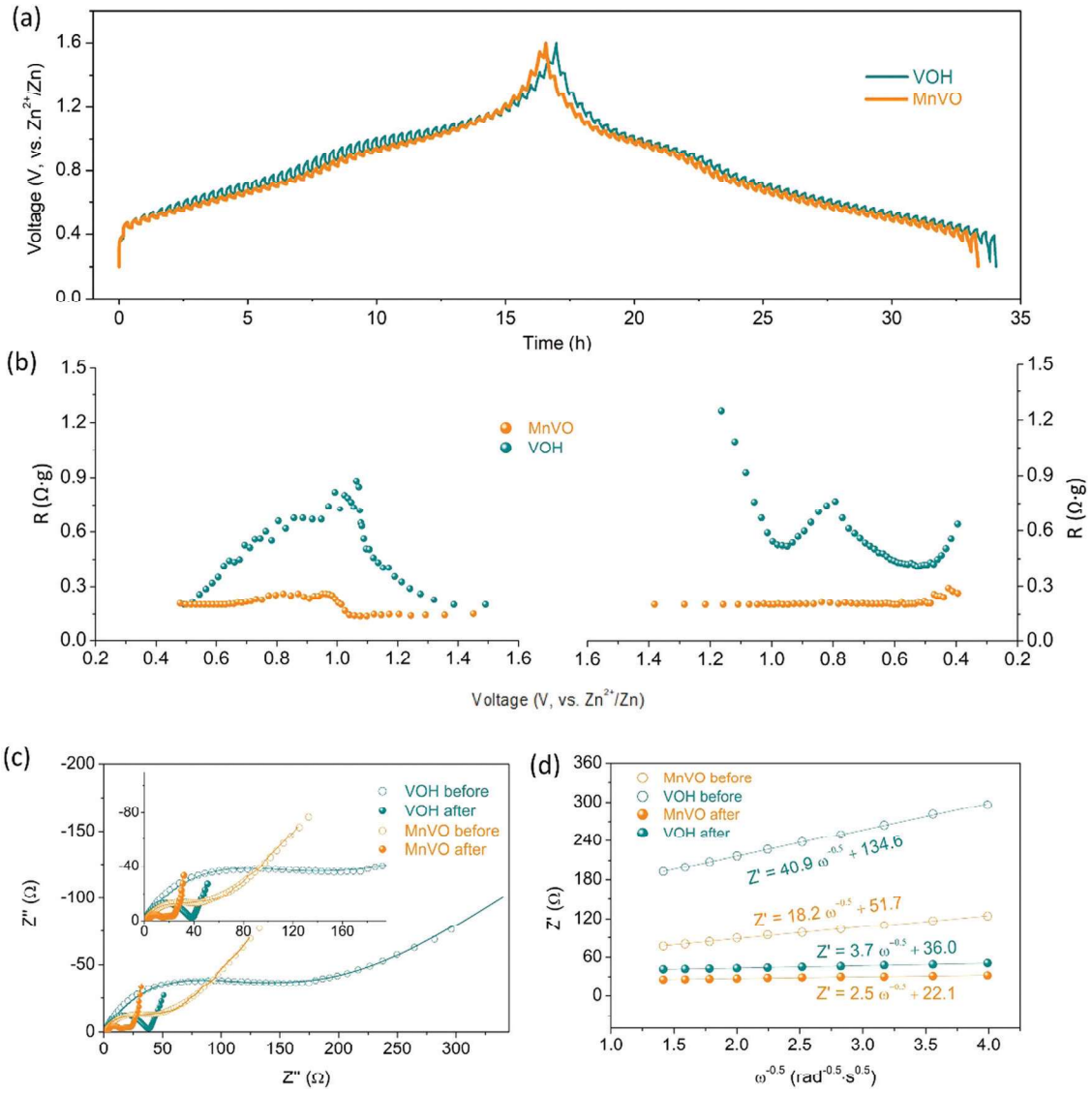

Fig. 6 (a) GITT plot collected at a current density of 50 mA h g^{-1}. (b) The reaction resistance during the charging and discharging process, the smaller resistances in MnVO suggest better charge transfer in the redox reaction. (c) EIS spectra of both samples with the simulation curves before and after the first 3 cycles with a small current density used for the GITT. (d) The relationship between the real part of impedance and low frequencies, smaller slopes of the linear tendency mean faster ion diffusion in the electrochemical processes.

Table 2 The charge transfer resistances and ion diffusion coefficients from the EIS tests

Sample ID	Label	R_{ct} (Ω)	$D_{Zn^{2+}}$ (cm^2 s^{-1})
VOH	Before cycling	177	1.20×10^{-14}
	After 3 cycles	38	1.46×10^{-12}
MnVO	Before cycling	63	6.07×10^{-14}
	After 3 cycles	24	3.22×10^{-12}

diffusion.[81] MnVO presents a CTR of 63 Ω in the initial state and the CTR decreases to 24 Ω after 3 cycles, while the CTRs of VOH are 177 and 38 Ω before and after cycling. The decrease of the CTRs after cycling might be attributed to the activation of materials and a small amount of trapped Zn^{2+} connecting the [VO_n] interlayers to provide more charge transfer pathways. The relationship between low-frequencies and the real part of impedance (Fig. 6d) can be used to calculate the Zn-ion diffusion coefficients[92] (details shown in the ESI†) and MnVO has a higher $D_{Zn^{2+}}$ of 3.22×10^{-12} compared to that of 1.46×10^{-12} cm^2 s^{-1} in VOH after the material activation. The lower RRs and CTRs and higher $D_{Zn^{2+}}$ in MnVO guarantee the fast redox reaction and stable crystal structure supported by pillar Mn(II) endow excellent cycling stability at a high current density of 4 A g^{-1} as shown in Fig. 4b.

Mn(II) expanded VOH achieves structural stability and reduces the reaction polarization during the repeated charge/discharge process; nickel and cobalt sulfates were also used as the raw materials to replace manganese sulfate in the synthesis processes to obtain the stabilized samples. The resulting powders exhibit similar XRD patterns as shown in Fig. 7a, suggesting three samples have similar crystal structures to MnVO as characterized

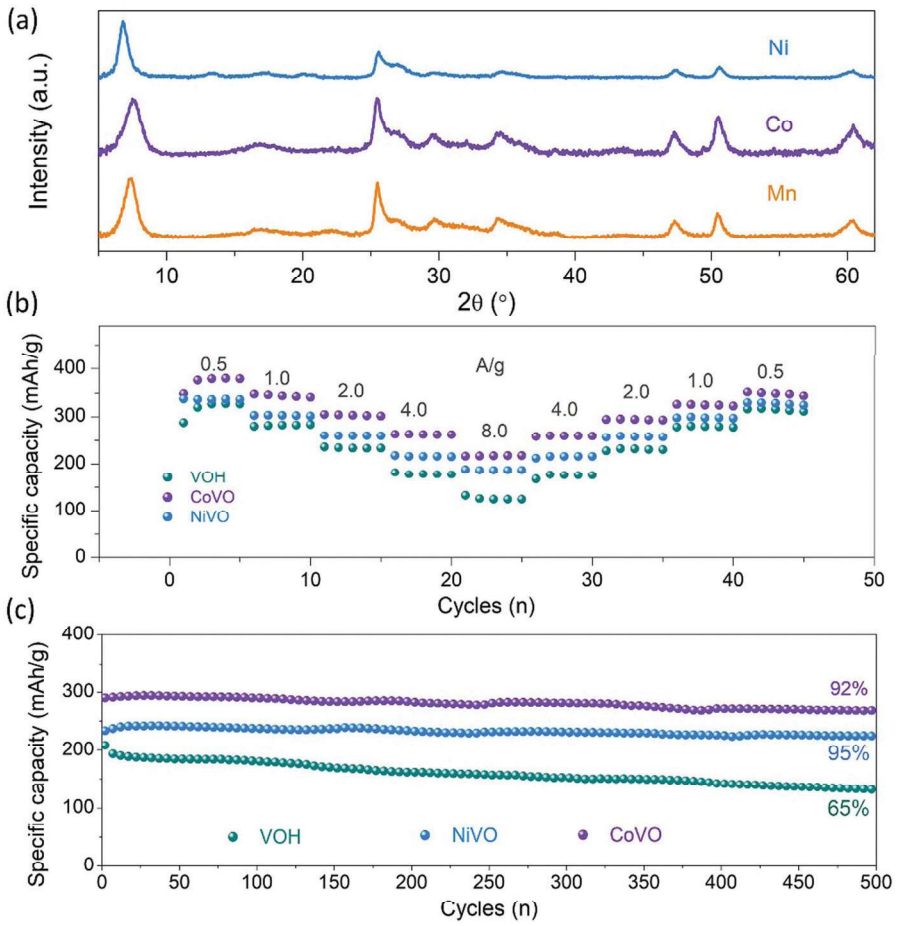

Fig. 7 (a) XRD patterns of NiVO, CoVO and the reference of MnVO. The similar diffraction patterns suggest the Ni(II) and Co(I) containing samples have the same structure as MnVO. (b) Rate capability and (c) cycling stability tested at 4 A g^{-1}. Divalent transition metal cations play the same role in stabilizing the crystal structures and enhancing the cycling stability in fast charge/discharge processes.

and analysed above. The comparisons of the rate capability and cycling stability are shown in Fig. 7b and c. Ni(II) vanadate (NiVO) and Co(II) vanadate (CoVO) deliver enhanced rate capability and display excellent cycling stability at 4 A g^{-1} and high capacity retentions of 92% and 95%, respectively. Those are higher than the 65% of VOH or ~80% of $Zn_{0.25}V_2O_5{\cdot}nH_2O$[36] or ~90% of $Na_2V_6O_{16}{\cdot}1.63H_2O$[92] previously reported, demonstrating TMC introduction can effectively improve the Zn-ion storage performance in hydrated vanadates. The disparities in the electrochemical performance of different TMC vanadates might be attributed to the ionic size of TMCs and their electronic structures will be studied in-depth in following work. Consequently, TMC introduction into hydrated vanadates is a general and effective strategy to improve the electrochemical performance for various multivalent ions' storage.

Conclusions

Expanding the interplanar spacing of hydrated vanadate by introduction of Mn(II) ions makes the cathode more thermally and structurally stable. Chemically inserted Mn(II) ions connect $[VO_n]$ layers by chemical bonds, work as pillars making a robust structure, and induce the formation of V^{4+} ions resulting in an expanded lattice spacing, which facilitates fast ion diffusion (3.22×10^{-12} cm^2 s^{-1}) and enhances the electrical conductivity. The MnVO cathode possesses a large storage capacity (260 mA h g^{-1}) at a higher discharge current density (4 A g^{-1}) compared to that of VOH. MnVO also demonstrates a capacity retention of 96% over 2000 cycles at 4 A g^{-1} compared to 65% of VOH over 500 cycles. Chemically inserted Mn(II) ions improved the reversibility by reducing the voltage polarization, resulting in an energy efficiency of 70% in the MnVO cathode battery, much higher than 40% for VOH at 4 A g^{-1} and with the open circuit voltage of the MnVO battery remaining at 1.36 V (85% of the cutoff voltage) after 50 days on the shelf. Divalent transition metal cations, such as Co and Ni, exhibit the same structures and stable cycling performance, suggesting that expanding VOH by introduction of TMCs is an effective and universal approach to improve or design high-performance cathode materials for aqueous Zn-ion and other multivalent ion batteries.

Conflicts of interest

There are no conflicts to declare.

Acknowledgements

This work was supported by the National Science Foundation (CBET-1803256). Part of this work was conducted at the Molecular Analysis Facility, a National Nanotechnology Coordinated Infrastructure site at the University of Washington which is supported in part by the National Science Foundation (grant NNCI-1542101), the University of Washington, the Molecular Engineering & Sciences Institute, and the Clean Energy Institute. The first author appreciates Mr Yong Chen and Mr Jun Qin from Neware Battery Testing Instruments for providing their technical support. MY and JY acknowledge the support from The Clean Energy Institute (CEI) at the University of Washington and the Inamori Foundation.

References

1 M. Li, J. Lu, Z. Chen and K. Amine, *Adv. Mater.*, 2018, **30**, 1800561.
2 A. Manthiram, J. C. Knight, S. T. Myung, S. M. Oh and Y. K. Sun, *Adv. Energy Mater.*, 2016, **6**, 1501010.
3 M. H. Han, E. Gonzalo, G. Singh and T. Rojo, *Energy Environ. Sci.*, 2015, **8**, 81–102.
4 M. S. Whittingham, *Science*, 1976, **192**, 1126–1127.
5 M. S. Whittingham, *J. Solid State Chem.*, 1979, **29**, 303–310.
6 M. Armand and J. M. Tarascon, *Nature*, 2008, **451**, 652–657.
7 X. Y. Lang, B. T. Liu, X. M. Shi, Y. Q. Li, Z. Wen and Q. Jiang, *Adv. Sci.*, 2016, **3**, 1500319.
8 A. Yoshino, *Angew. Chem., Int. Ed.*, 2012, **51**, 5798–5800.
9 N. A. Godshall, I. D. Raistrick and R. A. Huggins, *Mater. Res. Bull.*, 1980, **15**, 561–570.
10 K. Mizushima, P. C. Jones, P. J. Wiseman and J. B. Goodenough, *Mater. Res. Bull.*, 1980, **15**, 783–789.
11 R. C. Massé, C. Liu, Y. Li, L. Mai and G. Cao, *Natl. Sci. Rev.*, 2017, **4**, 26–53.
12 X. Liu, D. Ren, H. Hsu, X. Feng, G. L. Xu, M. Zhuang, H. Gao, L. Lu, X. Han, Z. Chu, J. Li, X. He, K. Amine and M. Ouyang, *Joule*, 2018, **2**, 2047–2064.
13 L. Suo, O. Borodin, T. Gao, M. Olguin, J. Ho, X. Fan, C. Luo, C. Wang and K. Xu, *Science*, 2015, **350**, 938–943.
14 Y. Yamada, K. Usui, K. Sodeyama, S. Ko, Y. Tateyama and A. Yamada, *Nat. Energy*, 2016, **1**, 16129.
15 P. Canepa, G. Sai Gautam, D. C. Hannah, R. Malik, M. Liu, K. G. Gallagher, K. A. Persson and G. Ceder, *Chem. Rev.*, 2017, **117**, 4287–4341.
16 M. Song, H. Tan, D. Chao and H. J. Fan, *Adv. Funct. Mater.*, 2018, **28**, 1802564.
17 R. J. Gummow, G. Vamvounis, M. B. Kannan and Y. He, *Adv. Mater.*, 2018, **30**, 1801702.
18 J. Muldoon, C. B. Bucur and T. Gregory, *Chem. Rev.*, 2014, **114**, 11683–11720.
19 G. Fang, J. Zhou, A. Pan and S. Liang, *ACS Energy Lett.*, 2018, **3**, 2480–2501.
20 Y. Li, J. Fu, C. Zhong, T. Wu, Z. Chen, W. Hu, K. Amine and J. Lu, *Adv. Energy Mater.*, 2019, **9**, 1802605.
21 A. Konarov, N. Voronina, J. H. Jo, Z. Bakenov, Y. K. Sun and S. T. Myung, *ACS Energy Lett.*, 2018, **3**, 2620–2640.
22 G. G. Yadav, J. W. Gallaway, D. E. Turney, M. Nyce, J. Huang, X. Wei and S. Banerjee, *Nat. Commun.*, 2017, **8**, 14424.
23 L. Wang, X. Cao, L. Xu, J. Chen and J. Zheng, *ACS Sustainable Chem. Eng.*, 2018, **6**, 16055–16063.
24 S. Zhao, B. Han, D. Zhang, Q. Huang, L. Xiao, L. Chen, D. G. Ivey, Y. Deng and W. Wei, *J. Mater. Chem. A*, 2018, **6**, 5733–5739.
25 B. Lee, H. R. Lee, H. Kim, K. Y. Chung, B. W. Cho and S. H. Oh, *Chem. Commun.*, 2015, **51**, 9265–9268.
26 M. Chamoun, W. R. Brant, C. W. Tai, G. Karlsson and D. Noréus, *Energy Storage Mater.*, 2018, **15**, 351–360.
27 H. Pan, Y. Shao, P. Yan, Y. Cheng, K. S. Han, Z. Nie, C. Wang, J. Yang, X. Li, P. Bhattacharya, K. T. Mueller and J. Liu, *Nat. Energy*, 2016, **1**, 16039.
28 N. Zhang, F. Cheng, J. Liu, L. Wang, X. Long, X. Liu, F. Li and J. Chen, *Nat. Commun.*, 2017, **8**, 405.
29 P. Hu, M. Yan, T. Zhu, X. Wang, X. Wei, J. Li, L. Zhou, Z. Li, L. Chen and L. Mai, *ACS Appl. Mater. Interfaces*, 2017, **9**, 42717–42722.
30 N. Zhang, Y. Dong, M. Jia, X. Bian, Y. Wang, M. Qiu, J. Xu, Y. Liu, L. Jiao and F. Cheng, *ACS Energy Lett.*, 2018, **3**, 1366–1372.
31 P. Senguttuvan, S. D. Han, S. Kim, A. L. Lipson, S. Tepavcevic, T. T. Fister, I. D. Bloom, A. K. Burrell and C. S. Johnson, *Adv. Energy Mater.*, 2016, **6**, 1600826.
32 J. Ding, Z. Du, L. Gu, B. Li, L. Wang, S. Wang, Y. Gong and S. Yang, *Adv. Mater.*, 2018, **30**, 1800762.
33 B. Sambandam, V. Soundharrajan, S. Kim, M. H. Alfaruqi, J. Jo, S. Kim, V. Mathew, Y. K. Sun and J. Kim, *J. Mater. Chem. A*, 2018, **6**, 3850–3856.
34 V. Soundharrajan, B. Sambandam, S. Kim, M. H. Alfaruqi, D. Y. Putro, J. Jo, S. Kim, V. Mathew, Y. K. Sun and J. Kim, *Nano Lett.*, 2018, **18**, 2402–2410.
35 B. Tang, G. Fang, J. Zhou, L. Wang, Y. Lei, C. Wang, T. Lin, Y. Tang and S. Liang, *Nano Energy*, 2018, **51**, 579–587.
36 D. Kundu, B. D. Adams, V. Duffort, S. H. Vajargah and L. F. Nazar, *Nat. Energy*, 2016, **1**, 16119.
37 Z. Liu, G. Pulletikurthi and F. Endres, *ACS Appl. Mater. Interfaces*, 2016, **8**, 12158–12164.
38 R. Trócoli and F. La Mantia, *ChemSusChem*, 2015, **8**, 481–485.
39 G. Kasiri, R. Trócoli, A. Bani Hashemi and F. La Mantia, *Electrochim. Acta*, 2016, **222**, 74–83.
40 L. Zhang, L. Chen, X. Zhou and Z. Liu, *Sci. Rep.*, 2015, **5**, 18263.
41 Y. Cheng, L. Luo, L. Zhong, J. Chen, B. Li, W. Wang, S. X. Mao, C. Wang, V. L. Sprenkle, G. Li and J. Liu, *ACS Appl. Mater. Interfaces*, 2016, **8**, 13673–13677.
42 M. S. Chae, J. W. Heo, S. C. Lim and S. T. Hong, *Inorg. Chem.*, 2016, **55**, 3294–3301.
43 W. Liu, J. Hao, C. Xu, J. Mou, L. Dong, F. Jiang, Z. Kang, J. Wu, B. Jiang and F. Kang, *Chem. Commun.*, 2017, **53**, 6872–6874.
44 H. Li, Q. Yang, F. Mo, G. Liang, Z. Liu, Z. Tang, L. Ma, J. Liu, Z. Shi and C. Zhi, *Energy Storage Mater.*, 2019, **19**, 94–101.
45 Q. Zhao, W. Huang, Z. Luo, L. Liu, Y. Lu, Y. Li, L. Li, J. Hu, H. Ma and J. Chen, *Sci. Adv.*, 2018, **4**, eaao1761.
46 D. Kundu, P. Oberholzer, C. Glaros, A. Bouzid, E. Tervoort, A. Pasquarello and M. Niederberger, *Chem. Mater.*, 2018, **30**, 3874–3881.

47 G. Fang, C. Zhu, M. Chen, J. Zhou, B. Tang, X. Cao, X. Zheng, A. Pan and S. Liang, *Adv. Funct. Mater.*, 2019, **29**, 1808375.
48 T. Gupta, A. Kim, S. Phadke, S. Biswas, T. Luong, B. J. Hertzberg, M. Chamoun, K. Evans-Lutterodt and D. A. Steingart, *J. Power Sources*, 2016, **305**, 22–29.
49 W. Xu, C. Sun, K. Zhao, X. Cheng, S. Rawal, Y. Xu and Y. Wang, *Energy Storage Mater.*, 2019, **16**, 527–534.
50 https://en.wikipedia.org/wiki/Abundance_of_elements_in_Earth%27s_crust.
51 M. Yan, P. He, Y. Chen, S. Wang, Q. Wei, K. Zhao, X. Xu, Q. An, Y. Shuang, Y. Shao, K. T. Mueller, L. Mai, J. Liu and J. Yang, *Adv. Mater.*, 2018, **30**, 1703725.
52 F. Ming, H. Liang, Y. Lei, S. Kandambeth, M. Eddaoudi and H. N. Alshareef, *ACS Energy Lett.*, 2018, **3**, 2602–2609.
53 Y. Yang, Y. Tang, G. Fang, L. Shan, J. Guo, W. Zhang, C. Wang, L. Wang, J. Zhou and S. Liang, *Energy Environ. Sci.*, 2018, **11**, 3157–3162.
54 C. Xia, J. Guo, P. Li, X. Zhang and H. N. Alshareef, *Angew. Chem., Int. Ed.*, 2018, **57**, 3943–3948.
55 C. C. Torardi, C. R. Miao, M. E. Lewittes and Z. Li, *J. Solid State Chem.*, 2002, **163**, 93–99.
56 J. Yao, Y. Li, R. C. Massé, E. Uchaker and G. Cao, *Energy Storage Mater.*, 2018, **11**, 205–259.
57 C. O'Dwyer, V. Lavayen, S. B. Newcomb, M. A. Santa Ana, E. Benavente, G. González and C. M. Sotomayor Torres, *J. Electrochem. Soc.*, 2007, **154**, K29–K35.
58 Q. Wei, J. Liu, W. Feng, J. Sheng, X. Tian, L. He, Q. An and L. Mai, *J. Mater. Chem. A*, 2015, **3**, 8070–8075.
59 D. McNulty, D. N. Buckley and C. O'Dwyer, *RSC Adv.*, 2016, **6**, 40932–40944.
60 C. L. Londoño-Calderón, C. Vargas-Hernández and J. F. Jurado, *Rev. Mex. Fis.*, 2010, **56**, 411–415.
61 S. Boukhalfa, K. Evanoff and G. Yushin, *Energy Environ. Sci.*, 2012, **5**, 6872–6879.
62 C. Sanchez, J. Livage and G. Lucazeau, *J. Raman Spectrosc.*, 1982, **12**, 68–72.
63 J. Lee, S. Badie, P. Srimuk, A. Ridder, H. Shim, S. Choudhury, Y. C. Nah and V. Presser, *Sustainable Energy Fuels*, 2018, **2**, 577–588.
64 S. V. Burdyukh, O. Y. Berezina, A. L. Pergament, L. A. Lugovskaya and Y. G. Kolyagin, *Thin Solid Films*, 2018, **656**, 22–29.
65 P. Remith and N. Kalaiselvi, *Nanoscale*, 2014, **6**, 14724–14732.
66 X. Li, C. Liu, C. Zhang, H. Fu, X. Nan, W. Ma, Z. Li, K. Wang, H. Wu and G. Cao, *ACS Appl. Mater. Interfaces*, 2016, **8**, 24629–24637.
67 S. Zhang, M. Hou, L. Hou and W. Ma, *Manganese and vanadium nanomaterial synthesis, application*, *China Pat.*, CN104876277A, 2015.
68 W. M. Haynes, *CRC Handbook of Chemistry and Physics*, Taylor & Francis, 93rd edn, 2012.
69 F. Liu, Z. Chen, G. Fang, Z. Wang, Y. Cai, B. Tang, J. Zhou and S. Liang, *Nano-Micro Lett.*, 2019, **11**, 25.
70 C. Li, P. Zheng, J. Li, H. Zhang, Y. Cui, Q. Shao, X. Ji, J. Zhang, P. Zhao and Y. Xu, *Angew. Chem., Int. Ed.*, 2003, **42**, 5063–5066.
71 H. Song, C. Liu, C. Zhang and G. Cao, *Nano Energy*, 2016, **22**, 1–10.
72 Y. Liu, M. Clark, Q. Zhang, D. Yu, D. Liu, J. Liu and G. Cao, *Adv. Energy Mater.*, 2011, **1**, 194–202.
73 Y. Wang, J. Li and Z. Wei, *J. Mater. Chem. A*, 2018, **6**, 8194–8209.
74 L. Chen, Y. Ruan, G. Zhang, Q. Wei, Y. Jiang, T. Xiong, P. He, W. Yang, M. Yan, Q. An and L. Mai, *Chem. Mater.*, 2019, **31**, 699–706.
75 X. Dai, F. Wan, L. Zhang, H. Cao and Z. Niu, *Energy Storage Mater.*, 2018, **17**, 143–150.
76 J. Wang, J. Polleux, J. Lim and B. Dunn, *J. Phys. Chem. C*, 2007, **111**, 14925–14931.
77 V. Augustyn, J. Come, M. A. Lowe, J. W. Kim, P. L. Taberna, S. H. Tolbert, H. D. Abruña, P. Simon and B. Dunn, *Nat. Mater.*, 2013, **12**, 518–522.
78 B. T. Liu, X. M. Shi, X. Y. Lang, L. Gu, Z. Wen, M. Zhao and Q. Jiang, *Nat. Commun.*, 2018, **9**, 1375.
79 Q. Pang, C. Sun, Y. Yu, K. Zhao, Z. Zhang, M. Voyles Paul, G. Chen, Y. Wei and X. Wang, *Adv. Energy Mater.*, 2018, **8**, 1800144.
80 M. H. Alfaruqi, V. Mathew, J. Song, S. Kim, S. Islam, D. T. Pham, J. Jo, S. Kim, J. P. Baboo, Z. Xiu, K. S. Lee, Y. K. Sun and J. Kim, *Chem. Mater.*, 2017, **29**, 1684–1694.
81 F. Wang, E. Hu, W. Sun, T. Gao, X. Ji, X. Fan, F. Han, X. Q. Yang, K. Xu and C. Wang, *Energy Environ. Sci.*, 2018, **11**, 3168–3175.
82 C. Liu, S. Wang, C. Zhang, H. Fu, X. Nan, Y. Yang and G. Cao, *Energy Storage Mater.*, 2016, **5**, 93–102.
83 S. H. Chung and A. Manthiram, *ACS Energy Lett.*, 2017, **2**, 1056–1061.
84 F. Beguin and E. Frackowiak, *Supercapacitors: Materials, Systems and Applications*, Wiley-VCH, 2013.
85 Y. Marcus, *Chem. Rev.*, 1988, **88**, 1475–1498.
86 P. v. d. Heide, *X-Ray Photoelectron Spectroscopy: An Introduction to Principles and Practices*, John Wiley & Sons, Inc., 2011.
87 X. Peng, X. Zhang, L. Wang, L. Hu, S. H. S. Cheng, C. Huang, B. Gao, F. Ma, K. Huo and P. K. Chu, *Adv. Funct. Mater.*, 2016, **26**, 784–791.
88 T. Wei, Q. Li, G. Yang and C. Wang, *J. Mater. Chem. A*, 2018, **6**, 20402–20410.
89 C. Zhu, G. Fang, J. Zhou, J. Guo, Z. Wang, C. Wang, J. Li, Y. Tang and S. Liang, *J. Mater. Chem. A*, 2018, **6**, 9677–9683.
90 Y. J. Zhu and C. S. Wang, *J. Phys. Chem. C*, 2010, **114**, 2830–2841.
91 D. W. Dees, S. Kawauchi, D. P. Abraham and J. Prakash, *J. Power Sources*, 2009, **189**, 263–268.
92 P. Hu, T. Zhu, X. Wang, X. Wei, M. Yan, J. Li, W. Luo, W. Yang, W. Zhang, L. Zhou, Z. Zhou and L. Mai, *Nano Lett.*, 2018, **18**, 1758–1763.